Scientific Research Publishing

Open Journal of Applied Sciences, 2025, 15(5), 1225-1244
https://www.scirp.org/journal/ojapps
ISSN Online: 2165-3925
ISSN Print: 2165-3917

Modeling and Control Analysis of Rope-Driven Continuous Robotic Arm Dynamics

Guang Hu, Weicai Quan*, Xiang Huang, Yucheng Zhou, Jianhao Chai, Yike Guo, Pengcheng Luo

National and Local Joint Engineering Laboratory for Marine Mineral Resources Exploration and Mining Equipment with Safety Technology, Hunan University of Science and Technology, Xiangtan, China
Email: *quanweicai@163.com

How to cite this paper: Hu, G., Quan, W.C., Huang, X., Zhou, Y.C., Chai, J.H., Guo, Y.K. and Luo, P.C. (2025) Modeling and Control Analysis of Rope-Driven Continuous Robotic Arm Dynamics. *Open Journal of Applied Sciences*, **15**, 1225-1244.
https://doi.org/10.4236/ojapps.2025.155085

Received: April 7, 2025
Accepted: May 16, 2025
Published: May 19, 2025

Abstract

In this paper, a rope-driven continuous robotic arm is taken as the research object, and its dynamic modeling and motion control methods are studied. Geometric analysis and coordinate transformation method are used to establish the kinematic model of the robot arm, and the Lagrangian method is used to construct the dynamics equation of the robot arm. The corresponding control system is designed based on the rope-driven robotic arm model, and the PID algorithm is used to realize the motion control of the robotic arm, and the simulation model is constructed using Simulink. The analysis shows that the actual joint trajectories of the rope-driven robotic arm under PID control can track the desired trajectories better, but due to the inherent strong coupling characteristics of the rope-driven robotic arm, the tracking errors of some joints show a tendency to accumulate over time. A fuzzy PID control algorithm is further proposed and simulation experiments are carried out, and the results show that after the introduction of the fuzzy control strategy, the joint angle tracking error of the rope-driven robotic arm is stabilized within the range of [−0.0014 rad, 0.0014 rad], which effectively solves the problem of error accumulation over time in PID control. And the position control error of the end of the robotic arm is stabilized in the range of [−0.6 mm, 0.8 mm], which verifies the correctness of the established dynamics model and the effective control of fuzzy PID control on the rope-driven continuous robotic arm.

Keywords

Rope-Driven Manipulator Arm, Lagrangian Dynamics, PID, Fuzzy Control

1. Introduction

The rope-driven continuous robotic arm shows good potential for application in

exploration, mining and rescue tasks. Compared with the traditional rigid robotic arm, which is not flexible enough to adapt to the narrow working environment, the rope-driven continuous robotic arm is better able to perform tasks in complex and narrow scenarios due to its high degree of freedom and flexibility. However, the special results of rope-driven robotic arms also make them highly coupled and nonlinear, which leads to many challenges in practical applications, such as complex dynamics modeling and difficulty in realizing precise motion control.

The study of dynamics modeling methods is of great significance in the field of rope-driven robotic arms, and there are various methods for establishing dynamics models, such as Newton-Euler method, Lagrange method [1], Kane method [2], etc. Xu Wenfu's research team [3] [4] innovatively combined the D-H parameter method with the Newton-Euler method. Scholars such as D. Axinte [5] proposed a new method to integrate the constant curvature model with the Newton-Euler method. However, Newton-Euler kinetic modeling is not intuitive enough to describe the complex coupled forces between the connecting rods of the rope-driven robotic arm. The Lagrange method describes the motion of a robotic arm by defining generalized coordinates in the configuration space. YANG *et al.* [6] proposed a modular dynamic modeling method for rope driven multi-stage flexible robotic arms. The NIU research team [7] established a closed model for axial contraction of a rope driven robotic arm based on Lagrange theory, and derived simplified closed analytical equations for bending and twisting based on Cosserat theory.

Different from the traditional rigid robotic arm, the rope-driven continuous robotic arm has the characteristics of multiple degrees of freedom and strong coupling, which makes it more difficult to realize its precise control. Shineng Geng and other scholars [8] established a kinematic mapping model based on the constant curvature assumption. Renda F *et al.* [9] proposed a research method based on the discretized Cosserat model. Fuzzy control has been widely used in real-time control systems due to its feature of state reasoning without the need for an accurate mathematical model, which can be realized only by input and output variables [10]. Goharimanesh and other scholars [11] proposed a novel control strategy combining the Cosserat rod model with fuzzy reinforcement learning and innovatively used Taguchi method and genetic algorithm to optimize the control parameters. Xu Wei *et al.* [12] designed a four-degree-of-freedom rope-driven continuous robotic arm and proposed a fuzzy controller with parameter self-tuning, which significantly improved the dynamic performance of the system.

In summary, this paper carries out research on the kinetic modeling and motion control method for a rope-driven continuous robotic arm. Geometric analysis and coordinate transformation methods are used to establish the kinematic model of the robotic arm, and the Lagrangian method is used to construct the kinetic equations of the robotic arm. A PID algorithm is used to realize the motion control of the robotic arm, and a fuzzy PID control algorithm is further proposed to realize the dynamic adjustment of the PID parameters by introducing fuzzy logic.

2. Description of the Structure of the Rope-Driven Robot Arm

The rope-driven continuous robotic arm studied in this paper adopts a modularized structure, which is mainly composed of three parts: drive unit, robotic arm body and transmission system. The arm body contains two joint modules with the same structure, and each module has two degrees of freedom: bending and rotating. Adopting glass fiber as the core material of the flexible support rod, a flexible support rod axially runs through seven equidistant support discs, including a base disc, an end disc and five intermediate support discs, as shown in Figure 1. The transmission system adopts three groups of super-elastic steel wire ropes as the power transmission medium, and the coordinated movement of the driving ropes can realize the continuous deformation and multi-attitude movement of the robotic arm in space.

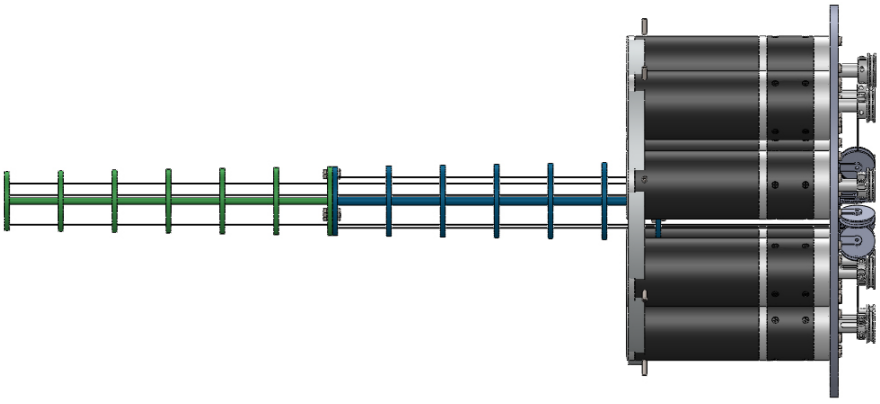

Figure 1. Structure of robotic arm.

Each joint module is bolted in series. The base disk of the first joint segment is fixed to the drive unit, while the base disk of the subsequent joint segment is connected to the end disk of the previous joint segment, as shown in Figure 2. The drive rope of each joint module passes through the base disk and each support disk of the joint segment in turn, and is finally fixed to the end disk.

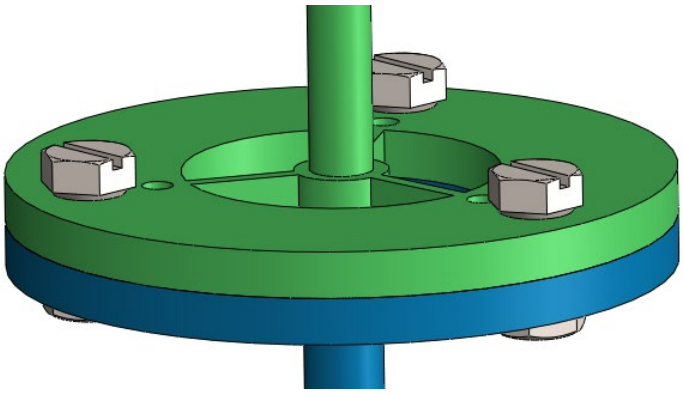

Figure 2. Schematic diagram of joint connection.

The support discs are made of aluminum alloy with a diameter of 40 mm and a total of 14. The support disc of the first segment robotic arm has 6 uniformly distributed drive rope perforations and 1 center positioning hole, while the support disc of the second segment robotic arm has 3 drive rope perforations and 1 center positioning hole, as shown in Figure 3. The drive ropes inside a single joint module are distributed using 120˚ equirectangular distribution, while the drive ropes between neighboring joints maintain a phase difference of 60˚. To facilitate the system description, the numbering rule of ni ($n = 1, 2$; $i = 1, 2, 3$) is used to denote the perforation hole position corresponding to the ith drive rope in the nth segment of the robotic arm. The center distance between all the drive rope threading holes and the center positioning holes is maintained at an equidistant distribution of 16 mm. Table 1 shows the configuration of the rope-driven robotic arm. Through the modularized series connection method, the number of joints can be extended according to the actual application requirements, so as to improve the degree of freedom of the robotic arm, enhance the spatial movement capability of the end-effector, and meet the operation requirements under complex working conditions.

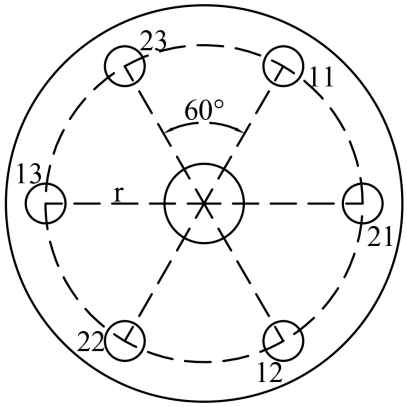

Figure 3. Schematic diagram of driving rope arrangement.

Table 1. Configuration of rope-driven continuous type robotic arm.

Configuration	Numerical
Single joint segment length: l	300 mm
Center support bar diameter: $d_{1,2,3}$	2 mm
Support disc radius: r	40 mm
Distance from crossing hole to center pole	16 mm
Number of joints	2
Number of single joint support discs	7
Total degrees of freedom	4

3. Kinematic Analysis of Rope-Driven Robotic Arm

Aiming at the structural characteristics of the rope-driven robotic arm, this study adopts a kinematic analysis method based on geometrical principles to establish a simplified geometrical model with the following basic assumptions [13]:

1) In the proposed robotic arm model, the strain-stress relationship of the superelastic wire rope is assumed to be linear and isotropic [14], the only external force on the robotic arm is the driving force, and the mechanical behavior of the backbone is similar to that of an Euler-Bernoulli beam; 2) the robotic arm disc is thin and hard, and the friction between the driving rope and the disc is negligible [15]; 3) since the gravitational potential energy is relatively small, the effect of gravitational potential energy can be neglected during the analysis; 4) The shape of the continuous type robotic arm is assumed to be a smooth and continuous curve, and the curvature of each trunk segment is kept constant; 5) The robotic arm is in static equilibrium [16]; 6) The center support rod and the driving rope are always perpendicular to each disk; 7) The center support rod of the robotic arm does not torsion, *i.e.*, only the advective kinetic energy of the driving rope, the support rod, and the disks are taken into account, while the rotational kinetic energy is not taken into account.

In constructing the single-joint kinematic model [17], it is first necessary to establish the reference coordinate systems {0} and {1} at the centers of the base disc and the end disc of the robotic arm, respectively. The *z*-axis of these two coordinate systems are both perpendicular to the plane of the corresponding discs and are set along the axial extension direction of the robotic arm, the *x*-axis is determined with the first drive rope perforation on the respective discs as the reference, and the *y*-axis is determined according to the right-hand rule to determine the spatial orientation, as shown in **Figure 4**.

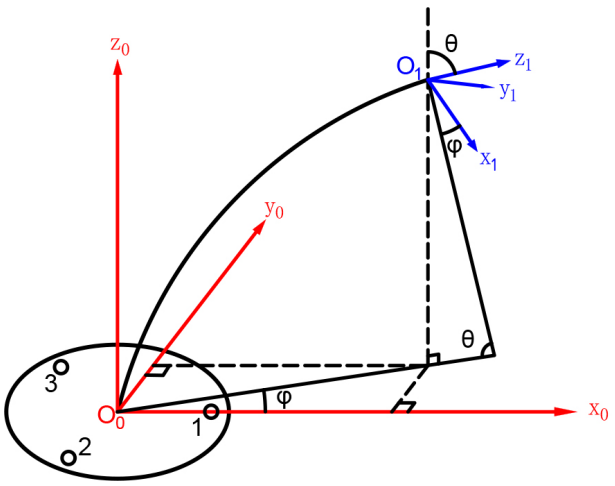

Figure 4. Geometric model of single joint of robotic arm.

Consider a rope-driven continuous robotic arm system consisting of N segments, each containing K support disks. Among them, the center points of the first and

last support discs of each segment are fixedly connected to the base coordinate system and the end coordinate system, respectively. Figure 5 illustrates the geometrical configuration of the nth segment of the robotic arm when it is bent [18], with the base coordinate system denoted by $O_{n-1}\text{-}X_{n-1}Y_{n-1}Z_{n-1}\left(n=1,2,\cdots,N\right)$ and the end coordinate system denoted by $O_n\text{-}X_nY_nZ_n\left(n=1,2,\cdots,N\right)$. By rotating the base coordinate system $O_{n-1}\text{-}X_{n-1}Y_{n-1}Z_{n-1}$ around its axis Z_{n-1} by an angle φ_n, the bending plane coordinate system $O_{rn}\text{-}X_{rn}Y_{rn}Z_{rn}$ of the robot arm can be established, and let θ_n denote the bending angle of the end of the robot arm, then the joint variable q of the N-segment rope-driven continuous robot arm can be denoted as $q=\left[\theta_1 \ \varphi_1 \ \theta_2 \ \varphi_2 \cdots \theta_N \ \varphi_N\right]^{\mathrm{T}}$.

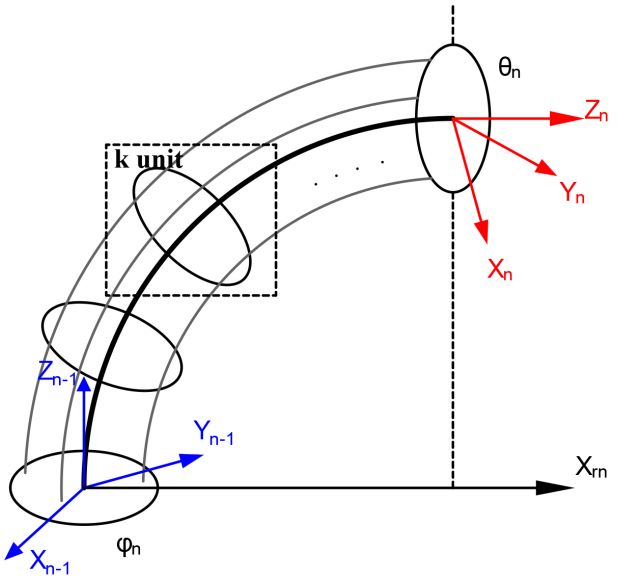

Figure 5. Geometric modeling of the nth segment of the robotic arm.

This special drive mode of rope drive determines that the kinematic analysis of rope-driven robotic arm needs to establish the mapping relationship among drive space, joint space and task space, as shown in Figure 6.

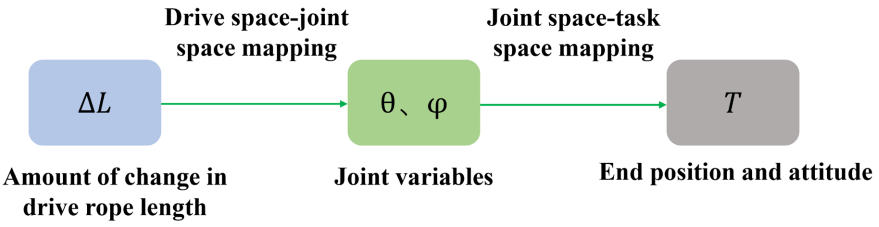

Figure 6. Spatial mapping relationship diagram of rope-driven robotic arm.

Joint space to drive space kinematic mapping, *i.e.*, when the bending angle and rotation angle of the joints are given, the length change amount of each drive rope can be solved. In the kinematic analysis, although the center support rod and the driving ropes both have the same bending angle, their radii of curvature differ due

to the radial offset, as shown in Figure 7. And the kinematic coupling effect brought by its unique rope arrangement must be fully considered. After the decoupling process, the length variation of the driving rope of the robotic arm and the joint variables can be expressed as follows

$$\Delta L_{ni} = \sum_{n=1}^{N} r\theta_n \cos\left(\varphi_n + \alpha_{ni}\right) \tag{1}$$

where in, ΔL_{ni} denotes the amount of change in the length of the ith drive rope of the nth section of the robotic arm, r denotes the center distance between the drive rope hole and the center support bar hole in the support disk, and α_{ni} denotes the distribution angle of the ith drive rope of the nth section in the support disk.

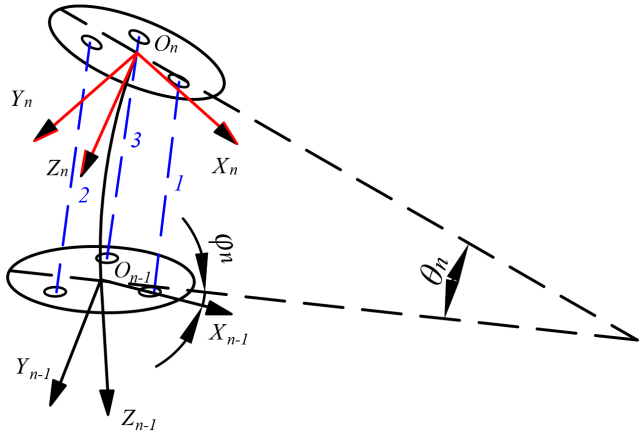

Figure 7. Schematic diagram of rope-driven robotic arm bending.

The kinematic mapping analysis of a rope-driven continuous robotic arm from the joint space to the task space refers to solving for the end position of the robotic arm in the task space when the joint variables $\theta_n\left(n=1,2\right)$ and $\varphi_n\left(n=1,2\right)$ are known. It can be described by the homogeneous transformation matrix T from the base coordinate system to the end coordinate system of each joint segment of the robotic arm

$$^{n-1}T_n = \begin{bmatrix} \sin^2\varphi_n + \cos^2\varphi_n\cos\theta_n & \cos\varphi_n\sin\varphi_n\left(\cos\theta_n - 1\right) & \cos\varphi_n\sin\theta_n & \frac{l}{\theta_n}\left(1-\cos\theta_n\right)\cos\varphi_n \\ \cos\varphi_n\sin\varphi_n\left(\cos\theta_n - 1\right) & \sin^2\varphi_n\cos\theta_n + \cos^2\varphi_n & \sin\varphi_n\sin\theta_n & \frac{l}{\theta_n}\left(1-\cos\theta_n\right)\sin\varphi_n \\ -\cos\varphi_n\sin\theta_n & -\sin\varphi_n\sin\theta_n & \cos\theta_n & \frac{l}{\theta_n}\sin\theta_n \\ 0 & 0 & 0 & 1 \end{bmatrix} \tag{2}$$

According to the chain rule in the analysis of robot kinematics, the homogeneous transformation matrix representation of the N-segment robotic arm can be obtained

$$^0T_N = {}^0T_1 \cdot {}^1T_2 \cdot {}^2T_3 \cdots {}^{N-1}T_N \tag{3}$$

Based on assumption conditions 1 - 6, denote the position homogeneous coordinates of any point on the center support bar of the nth section of the robotic arm with respect to the base coordinate system O_0-$X_0Y_0Z_0$ of the robotic arm as $r_{n0}=\left[x_n\ y_n\ z_n\ 1\right]^{\mathrm{T}}$, and the position homogeneous coordinates with respect to the end coordinate system O_{n-1}-$X_{n-1}Y_{n-1}Z_{n-1}$ of the (n-1)th section as $r_{n1}=\left[x_{n1}\ y_{n1}\ z_{n1}\ 1\right]^{\mathrm{T}}$, where

$$\begin{aligned} x_{n1} &= \frac{l}{\theta_n}\left(1-\cos\frac{s_n\theta_n}{l}\right)\cos\varphi_n \\ y_{n1} &= \frac{l}{\theta_n}\left(1-\cos\frac{s_n\theta_n}{l}\right)\sin\varphi_n \\ z_{n1} &= \frac{l}{\theta_n}\sin\frac{s_n\theta_n}{l} \end{aligned} \tag{4}$$

where s_n denotes the arc length of the point from the center point of the first support disk.

The transformation relation between the position coordinates r_{n0} and r_{n1} is expressed as

$$r_{n0} = {}^{0}T_{n-1}\cdot r_{n1} \tag{5}$$

4. Rope-Driven Robotic Arm Dynamics Modeling

Due to the need for dynamic modeling, the rope-driven robotic arm model is simplified by rigid-body equivalence in this paper. The supporting disc in the nth section of the robotic arm, as well as the center support rod and the driving rope connected to it, are regarded as a basic unit, as shown in Figure 5. In the kth unit, the center support rod is equivalent to a lightweight connecting rod, while the center of mass of this unit is assumed to be located at the center of the supporting disc. This simplified method significantly reduces the computational complexity while ensuring the accuracy of the model.

4.1. Calculation of Kinetic Energy of Rope-Driven Robot Arm

Based on assumption 7, the kinetic energy of each segment of the robotic arm can be expressed as the sum of the kinetic energy of each unit, and let s_{nk} denote the arc length parameter at the center-of-mass point of the kth unit on the nth segment, which is mathematically expressed as

$$s_{nk} = \frac{k}{K}l \tag{6}$$

where K denotes the number of support disks for each segment of the arm, and l denotes the length of the center support bar for each segment of the arm.

Substituting Equation (6) into Equations (4) and (5) yields a homogeneous coordinate representation of the kth cell center of mass point on the nth segment with respect to the coordinate system O_0-$X_0Y_0Z_0$

$$r_{nk0}=\left[x_{nk}\ y_{nk}\ z_{nk}\ 1\right]^{\mathrm{T}} \tag{7}$$

Deriving Equation (7) for time *t*, the *k*th cell center-of-mass velocity is expressed as

$$v_{nk0} = \begin{bmatrix} \dot{x}_{nk} & \dot{y}_{nk} & \dot{z}_{nk} & 0 \end{bmatrix}^{\mathrm{T}} = A_{nk} \cdot \dot{q}_n \tag{8}$$

where $\dot{q}_n$ is the *k*th cell center-of-mass joint velocity matrix on the *n*th segment, which has dimension 2×1, and A_{nk} is the matrix of coefficients corresponding to the joint velocities, which has dimension 4×2.

According to the kinetic energy formula, the expression for the kinetic energy of the *k*th cell center of mass point on the *n*th segment is given by

$$\begin{aligned} T_{nk} &= \frac{1}{2} m_{nk} v_{nk0}^{\mathrm{T}} v_{nk0} \\ &= \frac{1}{2} m_{nk} \dot{q}_n^{\mathrm{T}} A_{nk}^{\mathrm{T}} I_{4\times 4} A_{nk} \dot{q}_n \\ &= \frac{1}{2} \dot{q}_n^{\mathrm{T}} \cdot \left(A_{nk}^{\mathrm{T}} I_{4\times 4} m_{nk} A_{nk} \right) \cdot \dot{q}_n \end{aligned} \tag{9}$$

$$m_{nk} = m_a + m_b + 3 \cdot (N - n + 1) m_c \tag{10}$$

where m_{nk} denotes the total mass of the *k*th unit on the *n*th segment, m_a, m_b, m_c denotes the mass of the center support bar, the support disk, and the drive rope of the unit, respectively, and $I_{4\times 4}$ denotes the unit matrix of 4×4.

The kinetic energy of a single segment of the arm is expressed as

$$\begin{aligned} T_n &= \sum_{k=1}^{K} T_{nk} \\ &= \frac{1}{2} \dot{q}_n^{\mathrm{T}} \cdot \left(\sum_{k=1}^{K} A_{nk}^{T} m_{nk} A_{nk} \right) \cdot \dot{q}_n \\ &= \frac{1}{2} \dot{q}_n^{\mathrm{T}} M_n \dot{q}_n \end{aligned} \tag{11}$$

Taking the first segment of the robotic arm as an example, the matrix form of Equation (11) is

$$T_{1k} = \frac{1}{2} \begin{bmatrix} \dot{\theta}_1 & \dot{\varphi}_1 \end{bmatrix} \cdot \begin{bmatrix} a_{1k} & a_{3k} & a_{5k} & 0 \\ a_{2k} & a_{4k} & a_{6k} & 0 \end{bmatrix} \cdot \begin{bmatrix} m_{1k} & & & \\ & m_{1k} & & \\ & & m_{1k} & \\ & & & m_{1k} \end{bmatrix} \cdot \begin{bmatrix} a_{1k} & a_{2k} \\ a_{3k} & a_{4k} \\ a_{5k} & a_{6k} \\ 0 & 0 \end{bmatrix} \cdot \begin{bmatrix} \dot{\theta}_1 \\ \dot{\varphi}_1 \end{bmatrix} \tag{12}$$

where a_{ik} denotes the coefficient corresponding to the velocity of each joint of the unit center of mass after the derivation of the coordinates with respect to time.

From Equations (9), (10) and (11), the kinetic energy equations for the entire rope-driven continuous type robotic arm are obtained

$$\begin{aligned} T &= \sum_{n=1}^{N} \sum_{k=1}^{K} T_{kn} \\ &= \sum_{n=1}^{N} \frac{1}{2} \dot{q}_n^{\mathrm{T}} M_n \dot{q}_n \\ &= \frac{1}{2} \dot{q}_1^{\mathrm{T}} M_1 \dot{q}_1 + \frac{1}{2} \dot{q}_2^{\mathrm{T}} M_2 \dot{q}_2 \end{aligned} \tag{13}$$

The matrix form of Equation (13) is expressed as

$$T=\frac{1}{2}\begin{bmatrix}\dot{q}_1^{\mathrm{T}} & \dot{q}_2^{\mathrm{T}}\end{bmatrix}\cdot\begin{bmatrix}M_1 & \\ & M_2\end{bmatrix}\cdot\begin{bmatrix}\dot{q}_1\\ \dot{q}_2\end{bmatrix} \tag{14}$$

where $M_n \in R^{2N\times 2N}$ is a symmetric positive definite matrix, where

$$M=\sum_{n=1}^{N}\sum_{k=1}^{K}A_{nk}^{\mathrm{T}}\cdot I_{4\times 4}\cdot m_{nk}\cdot A_{nk} \tag{15}$$

Taking the first segment of the robotic arm as an example, when $k = 1$, the expression for the mass matrix M is

$$\begin{aligned}M_{11}&=\begin{bmatrix}a_{11} & a_{31} & a_{51} & 0\\ a_{21} & a_{41} & a_{61} & 0\end{bmatrix}\cdot\begin{bmatrix}m_{11} & & & \\ & m_{11} & & \\ & & m_{11} & \\ & & & m_{11}\end{bmatrix}\cdot\begin{bmatrix}a_{11} & a_{21}\\ a_{31} & a_{41}\\ a_{51} & a_{61}\\ 0 & 0\end{bmatrix}\\ &=\begin{bmatrix}a_{11}^2m_{11}+a_{31}^2m_{11}+a_{51}^2m_{11} & a_{11}a_{21}m_{11}+a_{31}a_{41}m_{11}+a_{51}a_{61}m_{11}\\ a_{11}a_{21}m_{11}+a_{31}a_{41}m_{11}+a_{51}a_{61}m_{11} & a_{21}^2m_{11}+a_{41}^2m_{11}+a_{61}^2m_{11}\end{bmatrix}\end{aligned} \tag{16}$$

When $k = 2$, this gives

$$\begin{aligned}M_{12}&=\begin{bmatrix}a_{12} & a_{32} & a_{52} & 0\\ a_{22} & a_{42} & a_{62} & 0\end{bmatrix}\cdot\begin{bmatrix}m_{12} & & & \\ & m_{12} & & \\ & & m_{12} & \\ & & & m_{12}\end{bmatrix}\cdot\begin{bmatrix}a_{12} & a_{22}\\ a_{32} & a_{42}\\ a_{52} & a_{62}\\ 0 & 0\end{bmatrix}\\ &=\begin{bmatrix}a_{12}^2m_{12}+a_{32}^2m_{12}+a_{52}^2m_{12} & a_{12}a_{22}m_{12}+a_{32}a_{42}m_{12}+a_{52}a_{62}m_{12}\\ a_{12}a_{22}m_{12}+a_{32}a_{42}m_{12}+a_{52}a_{62}m_{12} & a_{22}^2m_{12}+a_{42}^2m_{12}+a_{62}^2m_{12}\end{bmatrix}\end{aligned} \tag{17}$$

When $k = 3, \cdots$

And so on until $k = 7$, and the same is true for solving the mass matrix M for the second segment of the robotic arm.

4.2. Calculation of the Potential Energy of a Rope-Driven Robot Arm

According to assumption 3, ignoring the gravitational potential energy of the robot arm and considering only its elastic potential energy, the elastic potential energy on the nth segment is

$$\begin{aligned}U_n&=\int_0^l\frac{E_1I_1}{2}\cdot\left(\frac{\theta_n}{l}\right)^2\mathrm{d}s+3\left(N-n+1\right)\cdot\int_0^l\frac{E_2I_2}{2}\cdot\left(\frac{\theta_n}{l}\right)^2\mathrm{d}s\\ &=\frac{E_1I_1\theta_n^2}{2l}+3\left(N-n+1\right)\frac{E_2I_2\theta_n^2}{2l}\end{aligned} \tag{18}$$

where E_1, E_2 is the modulus of elasticity of the support rod and drive rope, respectively, and I_1, I_2 is the moment of inertia of the support rod and drive rope, respectively.

The total potential energy of the rope-driven continuous type robot arm is expressed as

$$U=\sum_{n=1}^{N}U_n=\left(\frac{E_1I_1}{2l}+\frac{3E_2I_2}{l}\right)\theta_1^2+\left(\frac{E_1I_1}{2l}+\frac{3E_2I_2}{2l}\right)\theta_2^2 \tag{19}$$

4.3. Rope-Driven Robotic Arm Generalized Force Calculation

The generalized force refers to the force or moment acting on the generalized coordinate position. Since each segment of the robotic arm has two degrees of freedom, the position and attitude of the robotic arm can be determined by applying the driving force only on the two driving ropes of each segment of the robotic arm, in addition to considering that the robotic arm ontology structure has central symmetry [19]. In a particular position case, the driving force F_1,F_2,F_3 exhibits spatial rotational symmetry during motion, *i.e.*, only two of the forces are effective in a certain determined position and attitude case. Based on the assumption condition 2 and combined with D'Alembert's principle, the generalized force calculation formula of the rope-driven continuous-type robotic arm can be obtained as

$$\begin{aligned}
\tau_1&=F_{11}\frac{\partial\Delta L_{11}}{\partial\theta_1}+F_{12}\frac{\partial\Delta L_{12}}{\partial\theta_1}+F_{21}\frac{\partial\Delta L_{21}}{\partial\theta_1}+F_{22}\frac{\partial\Delta L_{22}}{\partial\theta_1}\\
\tau_2&=F_{11}\frac{\partial\Delta L_{11}}{\partial\varphi_1}+F_{12}\frac{\partial\Delta L_{12}}{\partial\varphi_1}+F_{21}\frac{\partial\Delta L_{21}}{\partial\varphi_1}+F_{22}\frac{\partial\Delta L_{22}}{\partial\varphi_1}\\
\tau_3&=F_{11}\frac{\partial\Delta L_{11}}{\partial\theta_2}+F_{12}\frac{\partial\Delta L_{12}}{\partial\theta_2}+F_{21}\frac{\partial\Delta L_{21}}{\partial\theta_2}+F_{22}\frac{\partial\Delta L_{22}}{\partial\theta_2}\\
\tau_4&=F_{11}\frac{\partial\Delta L_{11}}{\partial\varphi_2}+F_{12}\frac{\partial\Delta L_{12}}{\partial\varphi_2}+F_{21}\frac{\partial\Delta L_{21}}{\partial\varphi_2}+F_{22}\frac{\partial\Delta L_{22}}{\partial\varphi_2}
\end{aligned} \tag{20}$$

where F_{ni} denotes the driving force provided by the ith driving rope of the nth segment of the continuous type robotic arm.

Combining Equations (1) and (20), it can be further deduced that

$$\begin{aligned}
\tau_1&=F_{11}r\cos\varphi_1+F_{12}r\cos\left(\varphi_1+\frac{2\pi}{3}\right)+F_{21}r\cos\varphi_1+F_{22}r\cos\left(\varphi_1+\frac{2\pi}{3}\right)\\
\tau_2&=-F_{11}\theta_1r\sin\varphi_1-F_{12}\theta_1r\sin\left(\varphi_1+\frac{2\pi}{3}\right)-F_{21}\theta_1r\sin\varphi_1-F_{22}\theta_1r\sin\left(\varphi_1+\frac{2\pi}{3}\right)\\
\tau_3&=F_{21}r\cos\varphi_2+F_{22}r\cos\left(\varphi_2+\frac{2\pi}{3}\right)\\
\tau_4&=-F_{21}\theta_2r\sin\varphi_2-F_{22}\theta_2r\sin\left(\varphi_2+\frac{2\pi}{3}\right)
\end{aligned} \tag{21}$$

4.4. Rope-Driven Robotic Arm Dynamics Model

According to robotics, it is known that for any mechanical system, the Lagrangian function is defined as the difference between the kinetic energy and the potential energy of the system, which leads to the dynamical equations of the system, *i.e.*, the Lagrangian equations of the second kind are

$$\frac{\mathrm{d}}{\mathrm{d}t}\frac{\partial T}{\partial \dot{q}_n}-\frac{\partial T}{\partial q_n}+\frac{\partial U}{\partial q_n}=\tau_n,\ n=1,2,\cdots,2N \tag{22}$$

where T and U are the kinetic and potential energies of the continuous type robotic arm, respectively, $\dot{q}_n$ is the corresponding joint velocity, and τ_n is the corresponding generalized force.

Substituting Equations (13), (19), and (21) into Equation (22), the equations for the dynamics of the rope-driven robotic arm can be obtained as

$$M(q)\ddot{q}+C(q,\dot{q})\dot{q}+K(q)q=\tau \tag{23}$$

where $M\in R^{2N\times 2N}$ is the inertia matrix of the robotic arm, $C\in R^{2N\times 2N}$ is the Koch force-centripetal force matrix, and $K\in R^{2N\times 2N}$ is the generalized stiffness matrix, which is expressed in matrix form as

$$\begin{aligned}&\begin{bmatrix}M_{11}&M_{12}&M_{13}&M_{14}\\M_{21}&M_{22}&M_{23}&M_{24}\\M_{31}&M_{32}&M_{33}&M_{34}\\M_{41}&M_{42}&M_{43}&M_{44}\end{bmatrix}\cdot\begin{bmatrix}\ddot{\theta}_1\\\ddot{\varphi}_1\\\ddot{\theta}_2\\\ddot{\varphi}_2\end{bmatrix}+\begin{bmatrix}C_{11}&C_{12}&C_{13}&C_{14}\\C_{21}&C_{22}&C_{23}&C_{24}\\C_{31}&C_{32}&C_{33}&C_{34}\\C_{41}&C_{42}&C_{43}&C_{44}\end{bmatrix}\cdot\begin{bmatrix}\dot{\theta}_1\\\dot{\varphi}_1\\\dot{\theta}_2\\\dot{\varphi}_2\end{bmatrix}\\&+\begin{bmatrix}K_{11}&K_{12}&K_{13}&K_{14}\\K_{21}&K_{22}&K_{23}&K_{24}\\K_{31}&K_{32}&K_{33}&K_{34}\\K_{41}&K_{42}&K_{43}&K_{44}\end{bmatrix}\cdot\begin{bmatrix}\theta_1\\\varphi_1\\\theta_2\\\varphi_2\end{bmatrix}=\begin{bmatrix}B_{11}&B_{12}&B_{13}&B_{14}\\B_{21}&B_{22}&B_{23}&B_{24}\\B_{31}&B_{32}&B_{33}&B_{34}\\B_{41}&B_{42}&B_{43}&B_{44}\end{bmatrix}\cdot\begin{bmatrix}F_1\\F_2\\F_3\\F_4\end{bmatrix}\end{aligned} \tag{24}$$

where $M_{ij},C_{ij},K_{ij},B_{ij}$ denotes the inertia matrix, the Coriolis-Centripetal matrix, the generalized stiffness matrix, and the matrix of coefficients in front of the generalized force terms of the robotic arm, respectively.

5. Motion Control and Simulation of Rope-Driven Robotic Arm

The design of the control system is crucial for the stable operation of the rope-driven robotic arm. Based on the constructed dynamic model of the rope-driven robotic arm, PID and fuzzy PID control strategies are used to control it, and simulation analysis is carried out using Simulink.

5.1. PID Control of Rope-Driven Robotic Arm

1) PID controller design

PID control is a linear control method based on error feedback, and its control algorithm can be expressed as follows

$$\begin{aligned}u(t)&=K_p\left[e(t)+\frac{1}{T_i}\int_0^t e(t)\mathrm{d}t+\frac{T_d\mathrm{d}e(t)}{\mathrm{d}t}\right]\\&=K_p e(t)+K_i\int_0^t e(t)\mathrm{d}t+K_d\frac{\mathrm{d}e(t)}{\mathrm{d}t}\end{aligned} \tag{25}$$

where: K_p, K_i, K_d are proportional, integral and differential gain coefficients, respectively.

The dynamic equations of the rope-driven continuous type robotic arm obtained from the above modeling are

$$\tau = M(q)\ddot{q} + C(q,\dot{q})\dot{q} + K(q)q \tag{26}$$

Set the tracking error to

$$\begin{aligned} e(t) &= q_d - q \\ \dot{e}(t) &= \dot{q}_d - \dot{q} \end{aligned} \tag{27}$$

where $e(t)$ is the deviation of the desired joint variable from the actual joint variable, q_d is the desired joint variable, and q is the actual joint variable.

The introduction of PID control results in

$$\begin{aligned} \tau &= M(q)\ddot{q} + C(q,\dot{q})\dot{q} + K(q)q + u(t) \\ &= M(q)\ddot{q} + C(q,\dot{q})\dot{q} + K(q)q + K_p e(t) + K_i \int_0^t e(t)\mathrm{d}t + K_d \frac{\mathrm{d}e(t)}{\mathrm{d}t} \end{aligned} \tag{28}$$

The block diagram of the rope-driven robotic arm PID control system is shown in Figure 8. Substituting Equation (27) into Equation (28) yields the complete expression of the PID control law for the rope-driven robotic arm as

$$\begin{aligned} \tau = M(q)\ddot{q} + C(q,\dot{q})\dot{q} + K(q)q + K_p(q_d - q) \\ + K_i \int_0^t (q_d - q)\mathrm{d}t + K_d(\dot{q}_d - \dot{q}) \end{aligned} \tag{29}$$

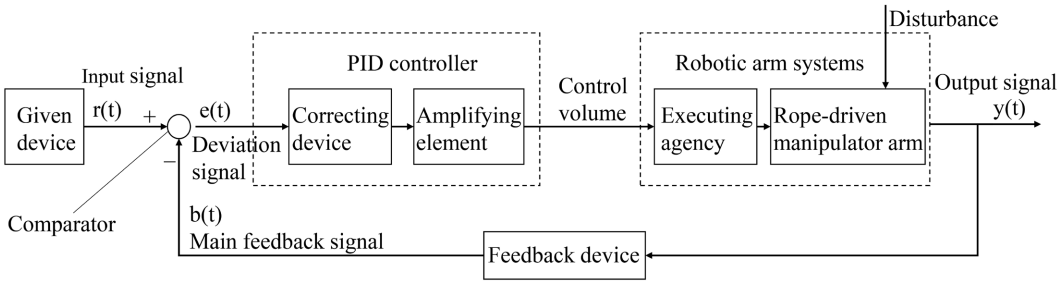

Figure 8. Block diagram of robotic arm PID control system.

2) PID control simulation

The trajectory tracking simulation of the rope-driven continuous robot arm is carried out according to the control system designed above. The simulation step size is taken as $\Delta t = 0.1$ s, and the total simulation time is set to $T = 24$ s; the initial joint angle and speed are set to 0; the desired trajectory is

$$\theta_{d1} = \frac{\pi}{3}\sin\frac{\pi}{4}t,\ \varphi_{d1} = \frac{\pi}{5}\sin\frac{\pi}{4}t,\ \theta_{d2} = \frac{\pi}{3}\sin\frac{\pi}{6}t,\ \varphi_{d2} = \frac{\pi}{5}\sin\frac{\pi}{6}t.$$

Setting the three parameter values of the PID controller, $K_p = 180$, $K_i = 22$, $K_d = 0.6$ the simulation results of PID control for trajectory tracking of Matlab-based rope-driven continuous robotic arm are shown in Figure 9, in which θ_n, φ_n on the left side of the figure represents the actual trajectory, $\theta_{dn}, \varphi_{dn}$ is the desired trajectory, and the right side figure represents the error between the actual joint angle and the desired joint angle.

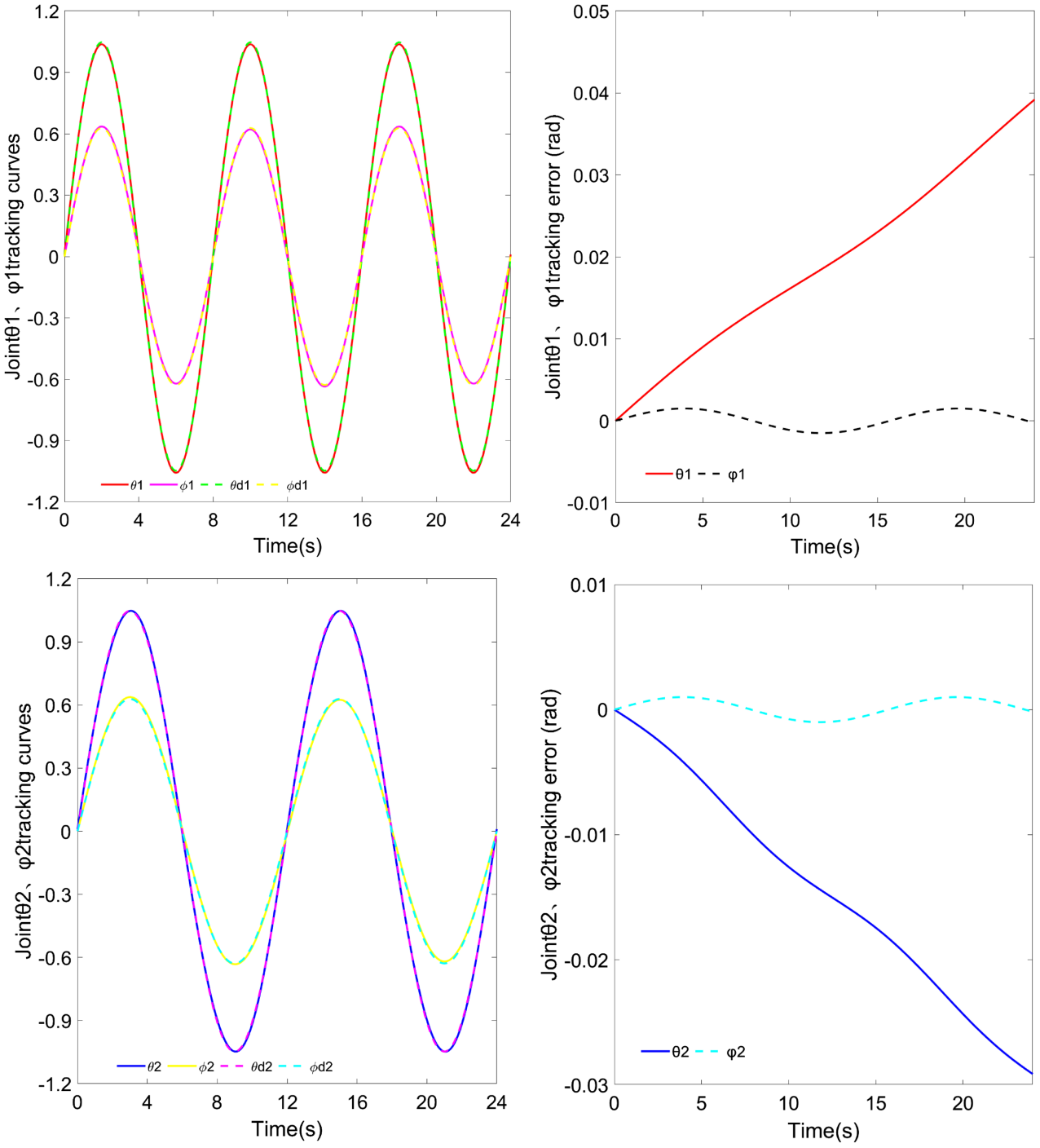

Figure 9. Trajectory tracking and error of each joint of the robotic arm.

According to the simulation results: the left image shows that the actual joint trajectories are able to track the desired trajectories well, with obvious deviations only when the corner changes. However, the error analysis curves on the right side show that the tracking errors of some joints show a tendency to accumulate over time, with the most significant error in the first joint near the base. This phenomenon is mainly due to the inherent strong coupling characteristics of the rope-

driven continuous robotic arm, where the motion of the rear joints significantly interferes with the front joints, especially the trajectory tracking accuracy of the first joint, which results in the accumulation of the error.

The above research results show that the PID control strategy demonstrates certain feasibility in the motion control of rope-driven continuous robotic arm, however, there are obvious limitations of the control method: the error of the robotic arm system shows a dispersion trend over time, which leads to a significant decrease in the control accuracy. In order to meet the demand for high-precision control, it is necessary to improve and optimize the existing control strategy.

5.2. Fuzzy PID Control of Rope-Driven Robotic Arm

Fuzzy logic control is added to the PID control, and a fuzzy PID controller is constructed by combining the fuzzy inference mechanism with the PID parameter adjustment to realize better control of the rope-driven continuous robotic arm, which is a nonlinear system.

1) Fuzzy PID controller design

In the fuzzy PID control system, the system deviation e and its rate of change de are used as the system inputs, which are mapped to the corresponding fuzzy set affiliations after the fuzzification process. Based on the fuzzy rule base constructed by the expert knowledge base, inference operations are performed on the fuzzified inputs to obtain the fuzzy outputs of the three control parameters. Subsequently, the defuzzification algorithm is used to convert the fuzzy outputs to the exact values $\Delta K_p, \Delta K_i, \Delta K_d$ for real-time adjustment of the proportional, integral and differential parameters of the PID controller as shown in Equation (30). The final generated control signal $u(t)$ acts on the controlled object to realize the dynamic optimal control of the system. The fuzzy PID control system for the rope-driven robotic arm is shown in Figure 10.

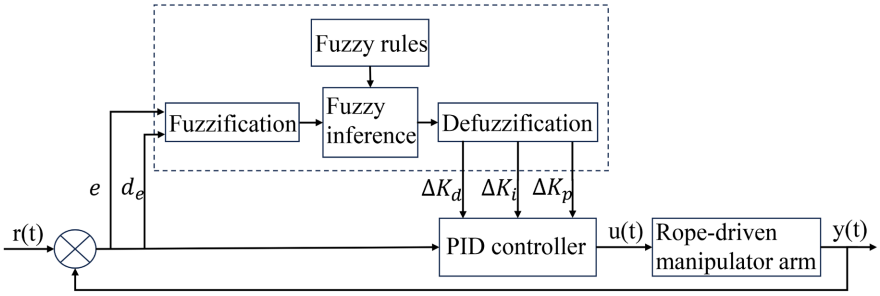

Figure 10. Fuzzy PID control system diagram for robotic arm.

The online correction formula for the PID control parameters is as follows

$$\begin{aligned} K_p &= K_{p0} + \Delta K_p \\ K_i &= K_{i0} + \Delta K_i \\ K_d &= K_{d0} + \Delta K_d \end{aligned} \tag{30}$$

Combining equations (25) and (30), the control law of the fuzzy PID controller is obtained as follows

$$\begin{aligned} u(t) &= K_p e(t) + K_i \int_0^t e(t)\mathrm{d}t + K_d \frac{\mathrm{d}e(t)}{\mathrm{d}t} \\ &= \left(K_{p0} + \Delta K_p\right) e(t) + \left(K_{i0} + \Delta K_i\right) \cdot \int_0^t e(t)\mathrm{d}t \\ &\quad + \left(K_{d0} + \Delta K_d\right) \frac{\mathrm{d}e(t)}{\mathrm{d}t} \end{aligned} \tag{31}$$

where K_{p0}, K_{i0}, K_{d0} is the initial value of the three PID parameters.

The design process of the fuzzy controller mainly includes the following key steps: firstly, determine the structural framework of the controller according to the input and output characteristics of the system; secondly, select the appropriate affiliation function to describe the fuzzy set of input and output variables, and establish the corresponding fuzzy rule base based on the experience of the experts; and lastly, clarify the fuzzy outputs on the basis of the determination of fuzzy inference mechanism [20].

In this study, the two-dimensional fuzzy controller structure is selected, the number of fuzzy sets of input and output variables are set to 5, the triangular and Gaussian composite form of the affiliation function is designed, the Mamdani inference algorithm is used, and the center of gravity method is selected as the defuzzification strategy to ensure that the control system is both stable and accurate, and the mathematical expression for the center of gravity method is

$$u = \frac{\int x\mu_N(x)\mathrm{d}x}{\int \mu_N(x)\mathrm{d}x} \tag{32}$$

2) Fuzzy PID control simulation

In order to facilitate the comparative analysis, the simulation parameters of the fuzzy PID controller are set to be consistent with the PID controller, and the simulation results are shown in **Figure 11**.

Simulation results show that the control system exhibits good trajectory tracking performance after the introduction of fuzzy control strategy. The joint angle control error is stabilized within the range of [−0.0014 rad, 0.0014 rad], which effectively solves the problem of error accumulation over time in PID control. Although the system still has obvious error fluctuations in the startup phase, the overall control effect is significantly improved. **Figure 12** shows the change of the deviation between the actual position and the desired position of the end of the robotic arm during trajectory tracking.

From the figure, it can be seen that the position control error of the end of the robotic arm is between [−0.6 mm, 0.8 mm]. This result indicates that the PID controller with the introduction of fuzzy control strategy can effectively enhance the control performance of the rope-driven continuous-type robotic arm and realize the expected control objective. The comparative analysis can confirm that the improved control scheme effectively enhances the adaptability of the robotic arm system to complex motion tasks.

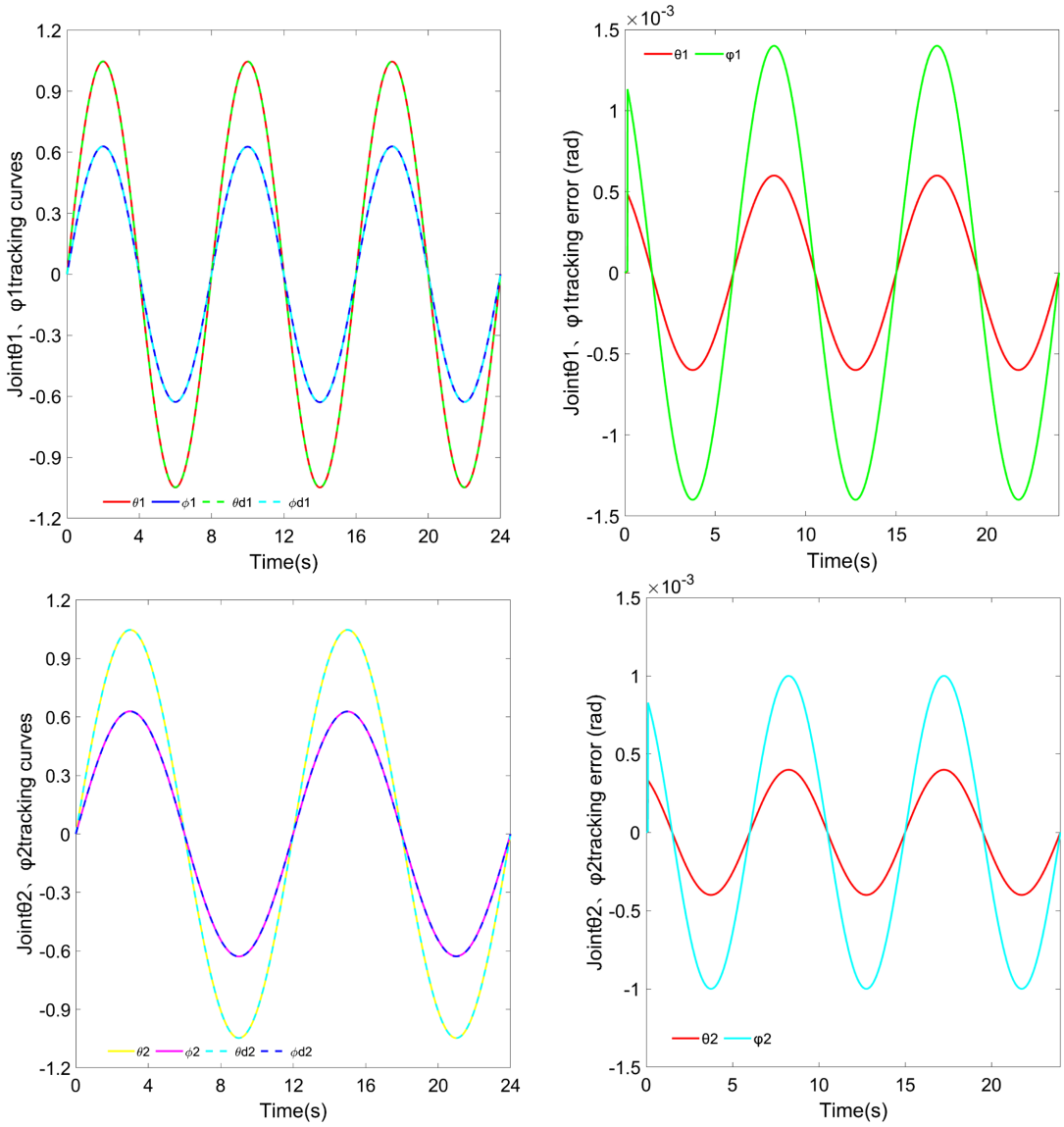

Figure 11. Trajectory tracking curves and errors for each joint of the robotic arm.

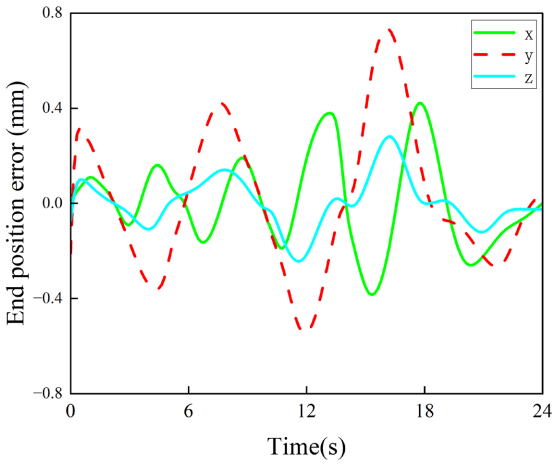

Figure 12. End position error of rope-driven continuous type robot arm.

6. Conclusion

This study addresses the dynamics modeling and control strategy of a rope-driven continuous type robotic arm. The kinematic model of the arm is established by geometric analysis and homogeneous coordinate transformation. For the dynamic characteristics of the rope-driven robotic arm system, the Lagrangian method is used for modeling, and the complete dynamic equations including inertial force, elastic force and driving force are deduced in detail. Based on the kinetic model of the rope-driven robotic arm, the PID controller is designed, and the simulation results show that the PID controller has certain feasibility for the tracking of the joint trajectory of the robotic arm, but there is a tendency for the joint angle error to diverge gradually with the extension of time. In order to suppress the gradual growth of error, fuzzy logic control is introduced to optimize the control system of the rope-driven continuous robotic arm, select fuzzy inputs and outputs, establish fuzzy rules, and design a fuzzy PID controller. The final results show that the joint tracking error of the PID control system with the addition of fuzzy control is between [−0.0014 rad, 0.0014 rad], which suppresses the trend of gradual increase of error, and the end position error is also stabilized at the millimeter level, which is within the acceptable range, which proves the correctness of the established model as well as the effective control of fuzzy PID control on the rope-driven continuous type robotic arm.

Sources and Participating Projects

1) National Natural Science Foundation of China (51709102), "Modeling and experimental study on the lengthening mechanism of variable-length underwater flexible cables".

2) National Key R&D Program of China, "Overall Technical Research on Intelligent Coordinated Control and Command System of Winch Group" (2022YFC2806901).

3) National Key R&D Program of China "Development of All-Sea Deep Subsea Coring Drilling Rig System" (2022YFC2805901).

4) National Key R&D Program of China: "System Integration and Sea Trial of All-Sea Deep Subsea Drilling Rig and Non-metallic Armored Umbilical Cable" (2022YFC2805904).

Conflicts of Interest

The authors declare no conflicts of interest regarding the publication of this paper.

References

[1] Falkenhahn, V., Mahl, T., Hildebrandt, A., Neumann, R. and Sawodny, O. (2015) Dynamic Modeling of Bellows-Actuated Continuum Robots Using the Euler-Lagrange Formalism. *IEEE Transactions on Robotics*, **31**, 1483-1496. https://doi.org/10.1109/tro.2015.2496826

[2] Yan, J. (2018) Review of Biomimetic Mechanism, Actuation, Modeling and Control

in Soft Manipulators. *Journal of Mechanical Engineering*, **54**, 1-14.

[3] Xu, W., Liu, T. and Li, Y. (2018) Kinematics, Dynamics, and Control of a Cable-Driven Hyper-Redundant Manipulator. *IEEE/ASME Transactions on Mechatronics*, **23**, 1693-1704. https://doi.org/10.1109/tmech.2018.2842141

[4] Liu, T., Mu, Z., Wang, H., Xu, W. and Li, Y. (2018) A Cable-Driven Redundant Spatial Manipulator with Improved Stiffness and Load Capacity. 2018 *IEEE/RSJ International Conference on Intelligent Robots and Systems* (*IROS*), Madrid, 1-5 October 2018, 6628-6633. https://doi.org/10.1109/iros.2018.8593679

[5] Dong, X., Axinte, D., Palmer, D., Cobos, S., Raffles, M., Rabani, A., *et al.* (2017) Development of a Slender Continuum Robotic System for on-Wing Inspection/Repair of Gas Turbine Engines. *Robotics and Computer-Integrated Manufacturing*, **44**, 218-229. https://doi.org/10.1016/j.rcim.2016.09.004

[6] Yang, J., Peng, H., Zhou, W., Zhang, J. and Wu, Z. (2021) A Modular Approach for Dynamic Modeling of Multisegment Continuum Robots. *Mechanism and Machine Theory*, **165**, Article 104429. https://doi.org/10.1016/j.mechmachtheory.2021.104429

[7] Niu, L., Ding, L., Gao, H., Su, Y., Deng, Z. and Liu, Z. (2019) Closed-Form Equations and Experimental Verification for Soft Robot Arm Based on Cosserat Theory. 2019 *IEEE/RSJ International Conference on Intelligent Robots and Systems* (*IROS*), 3-8 November 2019, 6630-6635. https://doi.org/10.1109/iros40897.2019.8968477

[8] Geng, S., Wang, Y., Wang, C. and Kang, R. (2018) A Space Tendon-Driven Continuum Robot. In: Tan, Y., Shi, Y. and Tang, Q., Eds., *Lecture Notes in Computer Science*, Springer International Publishing, 25-35. https://doi.org/10.1007/978-3-319-93818-9_3

[9] Renda, F., Cacucciolo, V., Dias, J. and Seneviratne, L. (2016) Discrete Cosserat Approach for Soft Robot Dynamics: A New Piece-Wise Constant Strain Model with Torsion and Shears. 2016 *IEEE/RSJ International Conference on Intelligent Robots and Systems* (*IROS*), Daejeon, 9-14 October 2016, 5495-5502. https://doi.org/10.1109/iros.2016.7759808

[10] Qi, P., Liu, C., Ataka, A., Lam, H.K. and Althoefer, K. (2016) Kinematic Control of Continuum Manipulators Using a Fuzzy-Model-Based Approach. *IEEE Transactions on Industrial Electronics*, **63**, 5022-5035. https://doi.org/10.1109/tie.2016.2554078

[11] Goharimanesh, M., Mehrkish, A. and Janabi-Sharifi, F. (2020) A Fuzzy Reinforcement Learning Approach for Continuum Robot Control. *Journal of Intelligent & Robotic Systems*, **100**, 809-826. https://doi.org/10.1007/s10846-020-01237-6

[12] Xu, W. (2018) Research on System Design and Motion Control of Rope-Driven Robot. Nanjing University of Aeronautics and Astronautics.

[13] He, B., Wang, Z., Li, Q., Xie, H. and Shen, R. (2013) An Analytic Method for the Kinematics and Dynamics of a Multiple-Backbone Continuum Robot. *International Journal of Advanced Robotic Systems*, **10**, Article 84. https://doi.org/10.5772/54051

[14] Nemat-Nasser, S. and Guo, W. (2006) Superelastic and Cyclic Response of NiTi SMA at Various Strain Rates and Temperatures. *Mechanics of Materials*, **38**, 463-474. https://doi.org/10.1016/j.mechmat.2005.07.004

[15] Xu, K. and Simaan, N. (2010) Intrinsic Wrench Estimation and Its Performance Index for Multisegment Continuum Robots. *IEEE Transactions on Robotics*, **26**, 555-561. https://doi.org/10.1109/tro.2010.2046924

[16] Xu, K. and Simaan, N. (2009) Analytic Formulation for Kinematics, Statics, and Shape Restoration of Multibackbone Continuum Robots via Elliptic Integrals. *Journal of Mechanisms and Robotics*, **2**, Article 011006.

https://doi.org/10.1115/1.4000519

[17] Feng, J. (2023) Research on the Design and Motion Control of Underwater Elephant Trunk-Like Rope-Driven Continuous Robotic Arm. Hunan University of Science and Technology.

[18] Ding, M., Yu, X., Wu, H., *et al.* (2022) Modeling and Control of a Multi-Section Cable-Driven Continuous Space Robotic Arm. *Journal of Nanjing University of Science and Technology*, **46**, 253-261.

[19] Li, Q., He, B. and Xie, H. (2012) Dynamic Modeling and Simulation of a Continuous Robot. *Mechanical Design and Research*, **28**, 18-22.

[20] Chiang, C. (2020) Optimization Study of Fuzzy PID Control for Trajectory Tracking of Six-Degree-of-Freedom Articulated Robots. Nanjing University of Aeronautics and Astronautics.